Extreme Values of Relative Distances for Spacecraft in Elliptic Displaced Orbits

Wei Wang[(1)], Giovanni Mengali[(2)], Alessandro A. Quarta[(2)] *, Jianping Yuan[(1)]

[(1)] *National Key Laboratory of Aerospace of Flight Dynamics, Northwestern Polytechnical University, 710072 Xi'an, People's Republic of China*

[(2)] *Department of Civil and Industrial Engineering, University of Pisa, I-56122 Pisa, Italy*

Abstract

This paper provides a framework to obtain a semi-analytical approximation of extreme values of relative distances between two spacecraft that cover elliptic displaced orbits. The relative motion is described in the rotating reference frame of the chief spacecraft and is parameterized with a new set of displaced orbital elements. The extreme values of the radial, along-track and cross-track distance are analytically evaluated (as roots of suitable algebraic equations) both for quasi-periodic orbits in the incommensurable case, and for periodic orbits in the 1:1 commensurable case. In particular, in the 1:1 commensurable case a Fourier series expansion is used to obtain a time-explicit expression of the relative motion. Finally, some illustrative examples are presented to validate the correctness of the proposed method.

Key words: Elliptic displaced orbits, Relative motion bounds, Formation flying

* Corresponding author.

Email addresses: 418362467@qq.com (Wei Wang[(1)]), g.mengali@ing.unipi.it (Giovanni Mengali[(2)]), a.quarta@ing.unipi.it (Alessandro A. Quarta[(2)]), jyuan@nwpu.edu.cn (Jianping Yuan[(1)]).

Nomenclature

a	=	semimajor axis of displaced orbit, [au]
b	=	semiminor axis of displaced orbit, [au]
E	=	eccentric anomaly, [rad]
f	=	true anomaly, [rad]
H	=	orbit displacement, [au]
$\hat{\boldsymbol{k}}$	=	unit vector of z-axis
i	=	inclination of displaced orbit, [rad]
$\hat{\boldsymbol{i}}$	=	unit vector of x-axis
J_h	=	Bessel function of the first kind of order h
$\hat{\boldsymbol{j}}$	=	unit vector of y-axis
M	=	mean anomaly, [rad]
n	=	mean motion, [rad/day]
O	=	Sun's center-of-mass
o	=	focus of displaced orbit
$\mathfrak{R}$	=	manifold
$\boldsymbol{r}$	=	spacecraft position vector in $\mathcal{T}_I$ (with $r = \|\boldsymbol{r}\|$), [au]
S	=	spacecraft center-of-mass
t	=	time, [days]
$\mathcal{T}_I$	=	inertial reference frame
$\mathcal{T}_P$	=	perifocal reference frame
$\mathcal{T}_R$	=	rotating reference frame
$\mathbb{T}_{PI}$	=	transformation matrix between $\mathcal{T}_P$ and $\mathcal{T}_I$
$\mathbb{T}_{PR}$	=	transformation matrix between $\mathcal{T}_P$ and $\mathcal{T}_R$
$\mathbb{T}_{P_D P_C}$	=	transformation matrix between $\mathcal{T}_{P_D}$ and $\mathcal{T}_{P_C}$

T_{ij}	=	(i,j) entry of matrix $\mathbb{T}_{P_D P_C}$
ρ_x, ρ_y, ρ_z	=	components of relative position vector in the chief's rotating frame, [au]
$\boldsymbol{\rho}$	=	relative position vector, [au]
Ω	=	right ascension of the ascending node of displaced orbit, [rad]
ω	=	argument of periapsis of displaced orbit, [rad]

Subscripts

C	=	chief
D	=	deputy
n	=	numerical solution

Superscripts

T	=	transpose
$\star$	=	extreme value
$\wedge$	=	unit vector

1 Introduction

The development of advanced materials, such as the graphene (Matloff, 2012), and the practical use of innovative propulsion system concepts, such as the photonic solar sail (Tsuda et al., 2011a,b; Mori et al., 2010; Johnson et al., 2011a, 2012, 2011b), have contributed to a growing interest towards non-Keplerian orbits (McKay et al., 2011; Mengali and Quarta, 2009), due to their potential benefits offered to astronomical missions. In particular, artificial Lagrange

orbits in a three-body dynamical system (McInnes et al., 1994; Baoyin and McInnes, 2005, 2006a,b) are capable of monitoring solar plasma storms (Prado et al., 1996), while displaced orbits in two-body problems (McInnes, 1997; McInnes and Simmons, 1992a,b) can be used as planet pole sitters (Ceriotti et al., 2014). In principle, a displaced orbit, that is, an orbit whose orbital plane does not contain the primary's center-of-mass, can be generated either by means of photonic solar sails (McInnes, 1998; Gong et al., 2008b), or by the more recent electric solar wind sails (Janhunen, 2004; Mengali and Quarta, 2009), whereas more conventional propulsion systems are known to be inadequate for these applications (McInnes, 1999).

In this context, most of the available literature is dedicated to the study of circular displaced orbits (McInnes, 1997; Ceriotti et al., 2014; Gong et al., 2008b; Mengali and Quarta, 2009) or to artificial Lagrange points (McInnes et al., 1994; Baoyin and McInnes, 2005, 2006a,b) in the restricted three-body problem, whereas elliptic displaced orbits have attracted smaller interest. However, some celestial bodies such as Mercury (or some near-Earth asteroids) track orbits with considerable eccentricity and, in that case, a full-time observation of their pole region could not be obtained using circular displaced orbits. An interesting option for those mission scenario is the use of elliptic displaced orbits. In particular, Gong and Li (2014) point out that a photonic solar sail with reflection control devices (electrochromic panels) could be able to achieve and maintain such kind of non-Keplerian orbit. This is possible by exploiting the fact that the mean optical properties of the sail's film can be adjusted, within some limits, by switching on or off the state of each electrochromic panel (Gong and Li, 2014; Mu et al., 2015a,b; Hu et al., 2015).

Moreover, scientific explorations of some celestial bodies that cover eccentric orbits, require multi-aspect observations that can only be accomplished using a formation of spacecraft. For instance, the interaction of solar wind with the magnetic field of Mercury is still, to some extent, an unknown phenomenon. An exhaustive comprehension of the magnetotail structure and dynamics of Mercury is possible only if a correlation between these two acting causes may

be found (Aliasi et al., 2015), which requires the simultaneous observation and measurement of both the magnetotail and the solar wind from different positions using multiple spacecraft. However, the only existing papers on solar sail relative motion around displaced orbits use a linearized mathematical model (Gong et al., 2007a, 2008a, 2007b, 2011), and thus can only be applied to small-distance and short-term missions. Especially for a large baseline formation flying, a nonlinear insight is indispensable for looking at some inherent properties of the formation structure, such as the bounds and the geometric topology of relative motion (Gurfil and Kholshevnikov, 2006), which might be useful for collision avoidance and communication analysis.

The aim of this paper is to give a comprehensive analysis of closed-form solutions and bounds of relative motion between elliptic displaced orbits, thus generalizing the recently developed theory (Wang et al., 2015) wherein the relative motion between circular displaced orbits has been investigated. A new set of displaced orbital elements is first introduced to describe an elliptic displaced orbit and to define its orientation with respect to an inertial reference frame. Based on the newly defined parameters, a closed-form solution expressed in the chief sail's rotating frame is derived without the need of solving or linearizing the relative dynamics. The relative motion emanated from the parametric solution is quasi-periodic for the incommensurable case and periodic for the commensurable case. In the commensurable case, the ratio between the mean motion of the two elliptic displaced orbits is a rational number, whereas for the incommensurable case the ratio is an irrational number. In both cases, the relative motion evolves along its invariant manifold that presents a well-defined accessible domain (Topputo, 2016; Mingotti et al., 2012).

The general solution is then used to look for the bounds along each coordinate axis assuming a small value of orbital eccentricity. For the 1:1 commensurable case, a first-order closed-form approximate solution is obtained, and the problem of looking for the bounds is transformed into that of calculating the roots of algebraic equations. The derived closed-form solutions are

of general applicability and do not suffer from the usual assumption of small relative distance between the two spacecraft, as in the linearized case.

2 Spacecraft relative position vector

Consider a spacecraft that covers a heliocentric displaced orbit using a continuous-thrust propulsion system and a suitable control law (Gong and Li, 2014). Such a non-Keplerian orbit is elliptic, with semimajor axis a and eccentricity $e \neq 0$ (both constant) and belongs to a plane $\mathcal{P}$ placed at a distance H from Sun's center-of-mass O. The special case of circular displaced orbit ($e = 0$) is thoroughly discussed in Wang et al. (2015), where the usefulness of a particular set of orbital elements has been pointed out to obtain a comprehensive description of the spacecraft dynamics along its orbit. By analogy with the Keplerian motion, let o be one of the two foci of the displaced orbit, and assume that such a point plays the same role of primary focus as it happens in a classic two-body problem (however, in this scenario the primary body is not placed at o). In particular, note that the segment O-o is orthogonal to the plane $\mathcal{P}$ of the displaced orbit. Accordingly, the spacecraft position along its elliptic orbit can be located using a sort of true anomaly f, measured anticlockwise from the line joining the focus o with the orbit's pericenter.

To formulate the problem conveniently, it is useful to introduce three right-handed reference frames, see Fig. 1. The first one is the classical heliocentric-ecliptic (inertial) reference frame $\mathcal{T}_I(O;\, x_I, y_I, z_I)$, where the plane (x_I, y_I) coincides with the ecliptic plane, the x_I axis points to the vernal equinox, and the z_I axis points to the north of celestial pole. The second coordinate system $\mathcal{T}_R(S;\, x_R, y_R, z_R)$ is a rotating reference frame centered at the spacecraft center-of-mass S, whose plane (x_R, y_R) coincides with plane $\mathcal{P}$, the x_R axis points from o to S, and z_R axis is positive in the direction of the spacecraft angular velocity vector. The unit vectors of $\mathcal{T}_R$ are $\hat{\boldsymbol{\imath}}_R$, $\hat{\boldsymbol{\jmath}}_R$, and $\hat{\boldsymbol{k}}_R$. Finally $\mathcal{T}_P(o;\, x_P, y_P, z_P)$ is a classical perifocal reference frame centered

at o, where the plane (x_P, y_P) coincides with plane $\mathcal{P}$, and x_P axis is directed from o to the periapsis of the elliptic displaced orbit.

Paralleling the classical approach of Keplerian motion, the orientation of the elliptic displaced orbit with respect to the inertial frame $\mathcal{T}_I$ is described by three Euler angles: the inclination $i \in [0,\, \pi]$, i.e. the angle between z_I-axis and the O-o line; the right ascension of the ascending node $\Omega \in [0,\, 2\,\pi]$, i.e. the angle between the line of nodes and the direction of x_I-axis; and the argument of periapsis $\omega \in [0,\, 2\,\pi]$, i.e. the angle between the line of nodes and the direction of the periapsis, see Fig. 1. In this context, the line of nodes is the intersection of plane $\mathcal{P}$ with plane $\mathcal{E}$, which is parallel to the ecliptic plane (x_I, y_I) and passes through the focus o of the displaced orbit. In the special case in which the plane of the displaced orbit is parallel to the ecliptic plane, the line of nodes is assumed to coincide with the line parallel to x_I and passing through the focus o.

Note that the absolute position vector $\boldsymbol{r}$ of the spacecraft, that is, its position vector evaluated in the inertial frame $\mathcal{T}_I$, can be written as a function of its true anomaly f as

$$\boldsymbol{r} = H\,\hat{\boldsymbol{k}}_R + \frac{a\,(1-e^2)}{1+e\,\cos f}\,\hat{\boldsymbol{\imath}}_R \tag{1}$$

where $H\,\hat{\boldsymbol{k}}_R$ is the position vector (in the inertial frame) of the focus o of the displaced orbit. Indeed, note that $\boldsymbol{r}$ is the vector from the Sun's center-of-mass to the spacecraft's center-of-mass. Therefore, the components of $\boldsymbol{r}$ in the rotating reference frame $\mathcal{T}_R$ are

$$[\boldsymbol{r}]_{\mathcal{T}_R} = \left[\frac{a\,(1-e^2)}{1+e\,\cos f},\quad 0,\quad H\right]^{\mathrm{T}} \tag{2}$$

Likewise, the components of vector $\boldsymbol{r}$ in the perifocal reference frame $\mathcal{T}_P$ (recall that the displaced orbit's plane does not contain the Sun's center-of-mass) are

$$[\boldsymbol{r}]_{\mathcal{T}_P} = [a\,(\cos E - e)\,,\quad b\,\sin E,\quad H]^{\mathrm{T}} \tag{3}$$

where $b = a\,\sqrt{1-e^2}$ is the semiminor axis of the elliptic displaced orbit, and E is the spacecraft

eccentric anomaly whose value, as a function of the true anomaly f, is given by the well known equation

$$\tan\frac{E}{2} = \sqrt{\frac{1-e}{1+e}}\,\tan\frac{f}{2} \tag{4}$$

Consider now the general scenario of two spacecraft flying along two different elliptic displaced orbits. The first spacecraft is referred to as the chief (subscript C), and the other as the deputy (subscript D), see Fig 2. The spacecraft relative position vector is given by

$$\boldsymbol{\rho} \triangleq \boldsymbol{r}_D - \boldsymbol{r}_C \tag{5}$$

where $\boldsymbol{r}_C$ (or $\boldsymbol{r}_D$) is the inertial position vector of the chief (or deputy). The components of $\boldsymbol{\rho}$ are usually expressed in the Cartesian space. However, such a choice provides little physical insight within a three-dimensional scenario, especially for emphasizing the extreme values of the spacecraft relative distances, i.e. the extreme values of each component of $\boldsymbol{\rho}$. For this reason, it is better to write the components of $\boldsymbol{\rho}$ as a function of both the true anomaly f and the geometrical characteristics, given by the set $\{a,\, e,\, \Omega,\, \omega,\, i,\, H\}$, of the two elliptic displaced orbits.

The components of $\boldsymbol{\rho}$ are now written in the chief's rotating frame $\mathcal{T}_{R_C}$, and three coordinate transformations are carried out to find the components of $\boldsymbol{r}_D$ in $\mathcal{T}_{R_C}$. To that end, the inertial frame $\mathcal{T}_I$ is used as an intermediate bridge (Gurfil and Kholshevnikov, 2006). The first transformation is from the deputy's perifocal frame $\mathcal{T}_{P_D}$ to the inertial frame $\mathcal{T}_I$, the second is from $\mathcal{T}_I$ to the chief's perifocal frame $\mathcal{T}_{P_C}$, and the last one is from $\mathcal{T}_{P_C}$ to $\mathcal{T}_{R_C}$. Taking into account (Battin, 1987) that the transformation matrix $\mathbb{T}_{PI}$ between $\mathcal{T}_P$ and $\mathcal{T}_I$ is a function of

the triplet $\{\Omega, i, \omega\}$ via the equation

$$\mathbb{T}_{PI}\left(\Omega, i, \omega\right) \triangleq \begin{bmatrix} (\cos\omega\cos\Omega - \sin\omega\cos i\sin\Omega) & (-\sin\omega\cos\Omega - \cos\omega\cos i\sin\Omega) & (\sin i\sin\Omega) \\ (\cos\omega\sin\Omega + \sin\omega\cos i\cos\Omega) & (\cos\omega\cos i\cos\Omega - \sin\omega\sin\Omega) & (-\sin i\cos\Omega) \\ \sin\omega\sin i & \cos\omega\sin i & \cos i \end{bmatrix} \tag{6}$$

and that the transformation matrix $\mathbb{T}_{PR}$ between the perifocal frame and the rotating frame is

$$\mathbb{T}_{PR}\left(f\right) = \begin{bmatrix} \cos f & \sin f & 0 \\ -\sin f & \cos f & 0 \\ 0 & 0 & 1 \end{bmatrix} \tag{7}$$

Eq. (5) provides

$$[\boldsymbol{\rho}]_{\mathcal{T}_{R_C}} = \mathbb{T}_{PR}(f_C)\,\mathbb{T}^{\mathrm{T}}_{P_CI}\left(\Omega_C, i_C, \omega_C\right)\,\mathbb{T}_{P_DI}\left(\Omega_D, i_D, \omega_D\right)\,[\boldsymbol{r}_D]_{\mathcal{T}_{P_D}} - [\boldsymbol{r}_C]_{\mathcal{T}_{R_C}} \tag{8}$$

where $[\boldsymbol{r}_D]_{\mathcal{T}_{P_D}}$ is given by Eqs. (3)-(4) as a function of $\{a_D, e_D, f_D, H_D\}$, and $[\boldsymbol{r}_C]_{\mathcal{T}_{R_C}}$ is given by Eq. (2) as a function of $\{a_C, e_C, f_C, H_C\}$. For the sake of conciseness, the eccentric anomaly E_D is used in place of the true anomaly f_D for the deputy, and the following shorthand notation is introduced

$$\mathbb{T}_{P_DP_C} \triangleq \mathbb{T}^{\mathrm{T}}_{P_CI}\left(\Omega_C, i_C, \omega_C\right)\,\mathbb{T}_{P_DI}\left(\Omega_D, i_D, \omega_D\right) \tag{9}$$

where $\mathbb{T}_{P_DP_C}$ represents the transformation matrix between the chief's perifocal frame and the deputy's perifocal frame.

Substituting Eqs. (2)–(3) and (6)–(7) into Eq. (8), the components ρ_x, ρ_y, and ρ_z of the relative position vector $\boldsymbol{\rho}$ in $\mathcal{T}_{R_C}$ can be written in terms of elliptic displaced orbit characteristics of

both the chief and the deputy spacecraft, viz.

$$\rho_x = a_D\,T_{11}\,\cos f_C\,\cos E_D + a_D\,T_{21}\,\sin f_C\,\cos E_D + b_D\,T_{12}\,\cos f_C\,\sin E_D + b_D\,T_{22}\,\sin f_C\,\sin E_D + (H_D\,T_{13} - a_D\,e_D\,T_{11})\cos f_C + (H_D\,T_{23} - a_D\,e_D\,T_{21})\sin f_C - \frac{a_C\,(1-e_C^2)}{1+e_C\,\cos f_C} \tag{10}$$

$$\rho_y = a_D\,T_{21}\,\cos f_C\,\cos E_D - a_D\,T_{11}\,\sin f_C\,\cos E_D + b_D\,T_{22}\,\cos f_C\,\sin E_D - b_D\,T_{12}\,\sin f_C\,\sin E_D + (H_D\,T_{23} - a_D\,e_D\,T_{21})\cos f_C + (a_D\,e_D\,T_{11} - H_D\,T_{13})\sin f_C \tag{11}$$

$$\rho_z = a_D\,T_{31}\,\cos E_D + b_D\,T_{32}\,\sin E_D + (H_D\,T_{33} - H_C - a_D\,e_D\,T_{31}) \tag{12}$$

where T_{ij} denotes the entry of row i and column j of matrix $\mathbb{T}_{P_D P_C}$, see Eqs. (76)–(84) in Appendix. Note that Eqs. (10)–(12) provide a parametric representation of the chief-deputy relative distance, with two angular coordinates (f_C, E_D) being the variables, thus comprising the invariant manifold $\mathfrak{R}$. In particular, Eqs. (10)–(12) remain valid for elliptic displaced orbits independent of the value of the orbital eccentricity.

There are two qualitatively different cases, depending on whether the mean motion of the two orbits, n_C and n_D respectively, are commensurable or not. Recall that in the commensurable case the ratio n_C/n_D is a rational number, whereas for the incommensurable case n_C/n_D is an irrational number. In the following sections, the bounds of each directional coordinate will be calculated analytically in both cases.

3 Bounds of incommensurable relative motion

As far as the incommensurable case is concerned, that is, when the ratio of mean motions is an irrational number, the relative motion evolving on the invariant manifold is open, but bounded, and is usually referred to as quasi-periodic. Due to its ergodic nature, the two angular variables in Eqs. (10)–(12), f_C and E_D, can be considered as independent of each other when differentiating the radial, along-track, and cross-track components with respect to them. In

other terms, the necessary conditions, which must be met to find the bounds of each component ρ_i, are

$$\frac{\partial \rho_i}{\partial f_C} = 0 \qquad \text{and} \qquad \frac{\partial \rho_i}{\partial E_D} = 0 \qquad \text{with} \qquad i = \{x,\, y,\, z\} \tag{13}$$

whose corresponding solutions in terms of the chief's true anomaly and the deputy's eccentric anomaly are referred to as $f_C = f_C^\star$ and $E_D = E_D^\star$, respectively. The bounds of the relative distances components are then calculated from Eqs. (10)–(12).

3.1 Radial bounds

According to Eq. (13), the extreme values of radial relative distance (i.e., the component of $\boldsymbol{\rho}$ along the x_R axis), are given by enforcing the necessary condition

$$\frac{\partial \rho_x}{\partial f_C} = 0 \qquad , \qquad \frac{\partial \rho_x}{\partial E_D} = 0 \tag{14}$$

In general, it is not possible to obtain a closed-form solution of $f_C^\star$ using the first one of Eqs. (14). However, assuming that $e_C \ll 1$, a first-order approximation of the chief's focus-spacecraft distance can be obtained using a Taylor series expansion of the last term in Eq. (10), viz.

$$\frac{a_C\,(1-e_C^2)}{1+e_C\,\cos f_C} \simeq a_C\,\left(1-e_C^2\right)\,(1-e_C\,\cos f_C) \tag{15}$$

Substituting Eq. (15) in Eq. (10), and then in Eqs. (14), the result is

$$\begin{aligned}&\varsigma_2\,\sin f_C\,\sin E_D - \varsigma_1\,\sin f_C\,\cos E_D + \varsigma_3\,\cos f_C \sin E_D + \varsigma_4\,\cos f_C\,\cos E_D + \varsigma_5\,\sin f_C \\ &+ \varsigma_6\,\cos f_C = 0\end{aligned} \tag{16}$$

$$\varsigma_3\,\sin f_C\,\cos E_D - \varsigma_4\,\sin f_C\,\sin E_D - \varsigma_1\,\cos f_C\,\sin E_D - \varsigma_2\,\cos f_C\,\cos E_D = 0 \tag{17}$$

where

$$\begin{aligned} &\varsigma_1 \triangleq a_D\, T_{11} \quad , \quad \varsigma_2 \triangleq -b_D\, T_{12} \quad , \quad \varsigma_3 \triangleq b_D\, T_{22} \quad , \quad \varsigma_4 \triangleq a_D\, T_{21} \quad , \\ &\varsigma_5 \triangleq a_D\, e_D\, T_{11} - H_D\, T_{13} - a_C\, e_C \quad , \quad \varsigma_6 \triangleq H_D\, T_{23} - a_D\, e_D\, T_{21} \end{aligned} \tag{18}$$

are constant coefficients depending on the characteristics of the two elliptic displaced orbits. Using the notation

$$\iota \triangleq \tan\frac{f_C}{2} \qquad , \qquad \upsilon \triangleq \tan\frac{E_D}{2} \tag{19}$$

Eqs. (16)-(17) are transformed into a new set of two nonlinear equations in two unknowns ι and υ, that is

$$\begin{aligned} &(\varsigma_4 - \varsigma_6)\, \iota^2\, \upsilon^2 + 2\, (\varsigma_1 + \varsigma_5)\, \iota\, \upsilon^2 - 2\, \varsigma_3\, \iota^2\, \upsilon - (\varsigma_4 + \varsigma_6)\, \iota^2 - (\varsigma_4 - \varsigma_6)\, \upsilon^2 \\ &+ 4\, \varsigma_2\, \iota\, \upsilon + 2\, (\varsigma_5 - \varsigma_1)\, \iota + 2\, \varsigma_3\, \upsilon + (\varsigma_4 + \varsigma_6) = 0 \end{aligned} \tag{20}$$

$$\varsigma_2\, \iota^2\, \upsilon^2 + 2\, \varsigma_3\, \iota\, \upsilon^2 - 2\, \varsigma_1\, \iota^2\, \upsilon - \varsigma_2\, \iota^2 - \varsigma_2\, \upsilon^2 + 4\, \varsigma_4\, \iota\, \upsilon - 2\, \varsigma_3\, \iota + 2\, \varsigma_1\, \upsilon + \varsigma_2 = 0 \tag{21}$$

Given an initial guess, Eqs. (20)–(21) can be solved as a function of ι and υ, and then the critical value of f_C and E_D can be obtained from Eq. (19). Due to the inherent singularities of the mapping from (f_C, E_D) to (ι, υ) in Eq. (19), it must be further checked whether $\iota \to \pm\infty$ and $\upsilon \to \pm\infty$ correspond to the extreme values. In this case, since $\iota \to \pm\infty$ when $f_C \to k\,\pi$ and $\upsilon \to \pm\infty$ when $E_D \to k\,\pi$ (where $k \in \mathbb{N}$), it is sufficient to investigate whether $\cos f_C = \pm 1$, $\sin f_C = 0$, $\cos E_D = \pm 1$, and $\sin E_D = 0$ correspond to extreme values by substituting them into Eqs. (16)-(17).

3.2 Along-track bounds

Bearing in mind Eq. (11), the necessary condition of Eq. (13) for the along-track motion leads to

$$\varsigma_4 \sin f_C \cos E_D + \varsigma_3 \sin f_C \sin E_D - \varsigma_2 \cos f_C \sin E_D + \varsigma_1 \cos f_C \cos E_D + \varsigma_6 \sin f_C - \varsigma_7 \cos f_C = 0 \tag{22}$$

$$\varsigma_2 \sin f_C \cos E_D + \varsigma_1 \sin f_C \sin E_D - \varsigma_4 \cos f_C \sin E_D + \varsigma_3 \cos f_C \cos E_D = 0 \tag{23}$$

where ς_1, ς_2, ..., ς_6 are given by Eq. (18) and

$$\varsigma_7 \triangleq a_D \, e_D \, T_{11} - H_D \, T_{13} \tag{24}$$

Taking into account Eq.(19), Eqs. (22)-(23) provide

$$(\varsigma_1 + \varsigma_7) \, \iota^2 \, \upsilon^2 + 2 \, (\varsigma_6 - \varsigma_4) \, \iota \, \upsilon^2 + 2 \, \varsigma_2 \, \iota^2 \, \upsilon + (\varsigma_7 - \varsigma_1) \, \iota^2 - (\varsigma_1 + \varsigma_7) \, \upsilon^2 + 4 \, \varsigma_3 \, \iota \, \upsilon + 2 \, (\varsigma_4 + \varsigma_6) \, \iota - 2 \, \varsigma_2 \, \upsilon + (\varsigma_1 - \varsigma_7) = 0 \tag{25}$$

$$\varsigma_3 \, \iota^2 \, \upsilon^2 - 2 \, \varsigma_2 \, \iota \, \upsilon^2 + 2 \, \varsigma_4 \, \iota^2 \, \upsilon - \varsigma_3 \, \iota^2 - \varsigma_3 \, \upsilon^2 + 4 \, \varsigma_1 \, \iota \, \upsilon + 2 \, \varsigma_2 \, \iota - 2 \, \varsigma_4 \, \upsilon + \varsigma_3 = 0 \tag{26}$$

Also, it must be further checked whether $\iota \to \pm\infty$ and $\upsilon \to \pm\infty$ correspond to extreme values using the same approach of radial bounds.

3.3 Cross-track bounds

To find the bounds of cross-track motion, the necessary condition of Eq. (13) results in

$$\varsigma_8 \sin E_D + \varsigma_9 \cos E_D = 0 \tag{27}$$

where

$$\varsigma_8 \triangleq a_D \, T_{31} \quad , \quad \varsigma_9 \triangleq b_D \, T_{32} \tag{28}$$

In this case, the critical values of the deputy's eccentric anomaly corresponding to the cross-track bounds can be directly written in an explicit form as:

$$E_D^\star = \begin{cases} (k + 1/2)\,\pi & \text{if} \quad \varsigma_8 = 0 \\ \\ k\,\pi - \arctan(\varsigma_9/\varsigma_8) & \text{if} \quad \varsigma_8 \neq 0 \end{cases} \tag{29}$$

with $k \in \mathbb{N}$, whereas the extreme values of z component are obtained by substituting Eq. (29) into Eq. (12).

4 Bounds in a 1:1 commensurable relative motion

In the commensurable case, that is, when the relative motion is periodic, an important scenario is the 1:1 commensurable relative motion. Indeed, in this case the period of the relative motion is the least common multiple of the two orbital periods, which often turns out to be unacceptably long if the condition of 1:1 is not satisfied. Therefore, the following discussion is confined to the 1:1 commensurable case only, and the condition $n_C = n_D \triangleq n$ is enforced.

Unlike the incommensurable relative motion where the critical time approaches infinity, the relative motion in the commensurable case exhibits periodicity and, therefore, the time t should be treated as the only independent variable when looking for the extreme values of the bounds. However, from Eqs. (10)–(12), the spacecraft relative distances are time-implicit. In this case, to obtain a time-explicit solution, the true anomaly and the eccentric anomaly must be written as an explicit function of time. To this end, first perform a nonlinear mapping from true anomaly f to mean anomaly M using Fourier series expansions (Battin, 1987):

$$\sin f = 2\sqrt{1-e^2} \sum_{h=1}^{\infty} \frac{\mathrm{d}J_h(he)}{\mathrm{d}e} \frac{\sin(h\,M)}{h} \tag{30}$$

$$\cos f = \frac{2\,(1-e^2)}{e} \sum_{h=1}^{\infty} J_h(he)\,\cos(h\,M) - e \tag{31}$$

where $J_h(\cdot)$ denotes the Bessel function of the first kind of order h defined as:

$$J_h(\nu) = \sum_{j=0}^{\infty} \frac{(-1)^j \, \nu^{h+2j}}{2^{h+2j} \, j! \, (h+j)!} \tag{32}$$

Likewise, the eccentric anomaly can be related to the mean anomaly as

$$\sin E = \sum_{h=1}^{\infty} \left[J_{h+1}(he) + J_{h-1}(he) \right] \frac{\sin(h\,M)}{h} = \frac{2}{e} \sum_{h=1}^{\infty} \frac{\sin(h\,M)}{h} J_h(h\,e) \tag{33}$$

$$\cos E = \sum_{h=1}^{\infty} \frac{1}{h} \left[J_{h-1}(he) - J_{h+1}(he) \right] \cos(h\,M) - \frac{e}{2} = \sum_{h=1}^{\infty} \frac{2\cos(h\,M)}{h^2} \frac{\mathrm{d}J_h(h\,e)}{\mathrm{d}e} - \frac{e}{2} \tag{34}$$

The generalized expansion theorem is now used to get

$$\frac{1-e^2}{1+e\,\cos f} = 1 + \frac{e^2}{2} - 2\,e \sum_{h=1}^{\infty} \frac{\mathrm{d}J_h(he)}{\mathrm{d}e} \frac{\cos(h\,M)}{h^2} \tag{35}$$

The first order term is sufficient for elliptic displaced orbits with small eccentricity, and Eqs. (30)–(31), (33)–(35) are rewritten as

$$\sin f \approx \sin M + e\,\sin(2\,M) + \mathcal{O}\left(e^2\right) \tag{36}$$

$$\cos f \approx -e + \cos M + e\,\cos(2\,M) + \mathcal{O}\left(e^2\right) \tag{37}$$

$$\sin E \approx \sin M + \frac{e}{2}\,\sin(2\,M) + \mathcal{O}\left(e^2\right) \tag{38}$$

$$\cos E \approx -\frac{e}{2} + \cos M + \frac{e}{2}\,\cos(2\,M) + \mathcal{O}\left(e^2\right) \tag{39}$$

$$\frac{a\,(1-e^2)}{1+e\,\cos f} \approx a\,(1-e\,\cos M) + \mathcal{O}\left(e^2\right) \tag{40}$$

Substituting Eqs. (36)–(40) into Eqs. (10)–(12) and neglecting second-order terms, an approx-

imate solution in terms of the two spacecraft mean anomalies is obtained as

$$\begin{aligned}\rho_x \approx & -\left(H_D T_{13} e_C + a_C\right) + \left(-3 a_D T_{11} e_D/2 + H_D T_{13} + a_C e_C\right) \cos M_C - a_D T_{11} e_C \cos M_D \\ & + \left(-3 a_D T_{21} e_D/2 + H_D T_{23}\right) \sin M_C - b_D T_{12} e_C \sin M_D + H_D T_{13} e_C \cos 2M_C + H_D T_{23} e_C \sin 2M_C \\ & + a_D T_{11} \cos M_C \cos M_D + b_D T_{12} \cos M_C \sin M_D + a_D T_{21} \sin M_C \cos M_D + b_D T_{22} \sin M_C \sin M_D \\ & + a_D T_{11} e_D \cos M_C \cos 2M_D/2 + b_D T_{12} e_D \cos M_C \sin 2M_D/2 + a_D T_{21} e_D \sin M_C \cos 2M_D/2 \\ & + b_D T_{22} e_D \sin M_C \sin 2M_D/2 + b_D T_{12} e_C \cos 2M_C \sin M_D + a_D T_{11} e_C \cos 2M_C \cos M_D \\ & + a_D T_{21} e_C \sin 2M_C \cos M_D + b_D T_{22} e_C \sin 2M_C \sin M_D \end{aligned} \tag{41}$$

$$\begin{aligned}\rho_y \approx & -H_D T_{23} e_C + \left(-3 a_D T_{21} e_D/2 + H_D T_{23}\right) \cos M_C - a_D T_{21} e_C \cos M_D \\ & + \left(3 a_D T_{11} e_D/2 - H_D T_{13}\right) \sin M_C - b_D T_{22} e_C \sin M_D + H_D T_{23} e_C \cos 2M_C - H_D T_{13} e_C \sin 2M_C \\ & + a_D T_{21} \cos M_C \cos M_D + b_D T_{22} \cos M_C \sin M_D - a_D T_{11} \sin M_C \cos M_D - b_D T_{12} \sin M_C \sin M_D \\ & + a_D T_{21} e_D \cos M_C \cos 2M_D/2 + b_D T_{22} e_D \cos M_C \sin 2M_D/2 - a_D T_{11} e_D \sin M_C \cos 2M_D/2 \\ & - b_D T_{12} e_D \sin M_C \sin 2M_D/2 + a_D T_{21} e_C \cos 2M_C \cos M_D + b_D T_{22} e_C \cos 2M_C \sin M_D \\ & - a_D T_{11} e_C \sin 2M_C \cos M_D - b_D T_{12} e_C \sin 2M_C \sin M_D \end{aligned} \tag{42}$$

$$\begin{aligned}\rho_z \approx & \left(-3 a_D T_{31} e_D/2 + H_D T_{33} - H_C\right) + a_D T_{31} \cos M_D + b_D T_{32} \sin M_D + a_D T_{31} e_D \cos 2M_D/2 \\ & + b_D T_{32} e_D \sin 2M_D/2 \end{aligned} \tag{43}$$

Assuming an initial mean anomaly $M_C(t_0) = M_D(t_0) = 0$, after some symbolic operations and simplifications, Eqs. (41)–(43) are written in a more compact form as

$$\rho_x \approx \sigma_0 + \sigma_c \cos(n\,t) + \sigma_s \sin(n\,t) + \sigma_{c2} \cos(2\,n\,t) + \sigma_{s2} \sin(2\,n\,t) + \sigma_{c3} \cos(3\,n\,t) + \sigma_{s3} \sin(3\,n\,t) \tag{44}$$

$$\rho_y \approx \tau_0 + \tau_c \cos(n\,t) + \tau_s \sin(n\,t) + \tau_{c2} \cos(2\,n\,t) + \tau_{s2} \sin(2\,n\,t) + \tau_{c3} \cos(3\,n\,t) + \tau_{s3} \sin(3\,n\,t) \tag{45}$$

$$\rho_z \approx \xi_0 + \xi_c \cos(n\,t) + \xi_s \sin(n\,t) + \xi_{c2} \cos(2\,n\,t) + \xi_{s2} \sin(2\,n\,t) \tag{46}$$

where the relevant coefficients are given in the Appendix, see Eqs. (85)–(103). Equations (44)–(46) provide a first-order approximate closed-form solution, which is very useful for understanding the nature of the relative motion due to its time-explicit property. Eqs. (44)–(46) also serve as a basis for studying the extreme values of the spacecraft relative distance along each coordinate axis, as is illustrated in the next sections.

To that end, the necessary condition to be met is

$$\frac{\partial \rho_i}{\partial t} = 0 \qquad \text{with} \qquad i = \{x,\, y,\, z\} \tag{47}$$

where the components ρ_i are given by Eqs. (44)–(46). Bearing in mind the structure of the three components of $\boldsymbol{\rho}$ in the chief's rotating frame, it is convenient to make the change of variable

$$s \triangleq \tan \frac{n\,t}{2} \qquad \text{with} \qquad n\,t \neq (2\,k+1)\,\pi \quad \text{and} \quad k \in \mathbb{N} \tag{48}$$

Correspondingly, the necessary condition of Eq. (47) becomes

$$\frac{\partial \rho_i}{\partial s} = 0 \qquad \text{if} \qquad n\,t \neq (2\,k+1)\,\pi \quad \text{with} \quad k \in \mathbb{N} \tag{49}$$

Once the positive values of s that satisfy Eq. (49) are found, the corresponding time values are obtained from Eq. (48). These time values, when substituted into Eqs. (44)–(46), provide a set of stationary values of ρ_i. The maximum or minimum of these stationary values can now be calculated along with the corresponding quantities $s^\star$ and $t^\star$ at which those extreme values are obtained.

Note that the change of variable in Eq. (48) can be performed only provided that $n\,t \neq (2\,k+1)\,\pi$. Therefore, it is necessary to check the generic component ρ_i in the particular case $n\,t = (2\,k+1)\,\pi$. To that end, it is necessary to substitute the condition $n\,t = (2\,k+1)\,\pi$ into

Eqs. (44)-(46). The corresponding expressions of the components of the position vector become

$$\rho_x \approx \sigma_0 - \sigma_c + \sigma_{c2} - \sigma_{c3} \tag{50}$$

$$\rho_y \approx \tau_0 - \tau_c + \tau_{c2} - \tau_{c3} \tag{51}$$

$$\rho_z \approx \xi_0 - \xi_c + \xi_{c2} \tag{52}$$

It is now sufficient to compare the values of the generic component ρ_i given by Eqs. (50)-(52) with those calculated using the necessary condition Eq. (49) in order to get (by direct comparison) the extreme values of each component of $\boldsymbol{\rho}$.

4.1 Radial bounds

Substituting Eq. (44) into Eq. (49) and recalling Eq. (48), the following polynomial equation in the variable s is obtained

$$\lambda_6\, s^6 + \lambda_5\, s^5 + \lambda_4\, s^4 + \lambda_3\, s^3 + \lambda_2\, s^2 + \lambda_1\, s + \lambda_0 = 0 \tag{53}$$

where λ_0, λ_1 , ..., λ_6 are constant coefficients given by

$$\lambda_0 = -\sigma_s + 2\,\sigma_{s2} - 3\,\sigma_{s3} \tag{54}$$

$$\lambda_1 = 2\,\sigma_c + 8\,\sigma_{c2} + 18\,\sigma_{c3} \tag{55}$$

$$\lambda_2 = -\sigma_s - 10\,\sigma_{s2} + 45\,\sigma_{s3} \tag{56}$$

$$\lambda_3 = 4\,\sigma_c - 60\,\sigma_{c3} \tag{57}$$

$$\lambda_4 = \sigma_s - 10\,\sigma_{s2} - 45\,\sigma_{s3} \tag{58}$$

$$\lambda_5 = 2\,\sigma_c - 8\,\sigma_{c2} + 18\,\sigma_{c3} \tag{59}$$

$$\lambda_6 = \sigma_s + 2\,\sigma_{s2} + 3\,\sigma_{s3} \tag{60}$$

where σ_s, σ_{s2}, σ_{s3}, σ_c, σ_{c2}, and σ_{c3} are given in the Appendix. Note that Eq. (53) is a sixth order polynomial equation whose real and positive roots can be easily numerically found. A similar procedure applies for the other two cases of ρ_y and ρ_z.

4.2 Along-track bounds

In this case the necessary condition of Eq. (47), where ρ_y is taken from Eq. (45), results in

$$\eta_6\, s^6 + \eta_5\, s^5 + \eta_4\, s^4 + \eta_3\, s^3 + \eta_2\, s^2 + \eta_1\, s + \eta_0 = 0 \tag{61}$$

where the constant coefficients η_0, η_1, ..., η_6 are given by (see also the Appendix)

$$\eta_0 = -\tau_s + 2\,\tau_{s2} - 3\,\tau_{s3} \tag{62}$$

$$\eta_1 = 2\,\tau_c + 8\,\tau_{c2} + 18\,\tau_{c3} \tag{63}$$

$$\eta_2 = -\tau_s - 10\,\tau_{s2} + 45\,\tau_{s3} \tag{64}$$

$$\eta_3 = 4\,\tau_c - 60\,\tau_{c3} \tag{65}$$

$$\eta_4 = \tau_s - 10\,\tau_{s2} - 45\,\tau_{s3} \tag{66}$$

$$\eta_5 = 2\,\tau_c - 8\,\tau_{c2} + 18\,\tau_{c3} \tag{67}$$

$$\eta_6 = \tau_s + 2\,\tau_{s2} + 3\,\tau_{s3} \tag{68}$$

4.3 Cross-track bounds

Finally, to get the cross-track bounds, the necessary condition of Eq. (47) with $\rho_i = \rho_z$ should be satisfied. Assuming that $n\,t \neq (2\,k+1)\,\pi$, the result is

$$\kappa_4\, s^4 + \kappa_3\, s^3 + \kappa_2\, s^2 + \kappa_1\, s + \kappa_0 = 0 \tag{69}$$

where the constant coefficients $\kappa_0, \kappa_1, \ldots, \kappa_4$ are

$$\kappa_0 = -\xi_s - 2\,\xi_{s2} \tag{70}$$

$$\kappa_1 = 2\,\xi_c + 8\,\xi_{c2} \tag{71}$$

$$\kappa_2 = 12\,\xi_{s2} \tag{72}$$

$$\kappa_3 = 2\,\xi_c - 8\,\xi_{c2} \tag{73}$$

$$\kappa_4 = \xi_s - 2\,\xi_{s2} \tag{74}$$

5 Case study

To verify the consistency of the proposed semi-analytical mathematical model, two illustrative examples are now discussed in which both the incommensurable and 1:1 commensurable case are considered.

5.1 Incommensurable case

Introduce a distance unit DU $\triangleq a_C$, and a time unit TU $\triangleq 1/n_C$. In order to obtain an incommensurable case, the semimajor axis of the deputy's elliptic displaced orbit is assumed to be $a_D = 1.02\,\mathrm{DU}$, so that the deputy's mean motion becomes $n_D = \sqrt{1/1.02^3}\,\mathrm{TU}^{-1}$ and the ratio n_C/n_D is an irrational number. In this scenario, the geometrical characteristics of the two displaced orbits are summarized in Tab. 1.

When the relative motion arrives at its radial, along-track and cross-track boundaries, the principal value of the corresponding (critical) true anomaly of the chief and eccentric anomaly of the deputy are listed in Tab. 2, along with the extreme values of the generic component ρ_i.

In fact, for the radial component of the relative position vector, from Eqs. (20)–(21) it is found that $\iota^\star = 0.0971$ and $\upsilon^\star = 0.0519$. On the other hand, for the along-track component of the relative position vector, from Eqs. (25)–(26) one obtains $\iota^\star = -1.4379$ and $\upsilon^\star = 0.0445$.

Figure 3 shows the relative motion (dotted line) and its invariant manifold $\mathfrak{R}$ along which it evolves in the chief-fixed rotating frame $\mathcal{T}_{R_C}$. Since the mean motions are incommensurable, the relative motion is quasi-periodic, and the relative orbit unfolds along a helix on the surface of $\mathfrak{R}$, winding round the whole region of the invariant manifold. In this case, Fig. 4 shows its projections on $(x_{R_C} - y_{R_C})$, $(x_{R_C} - z_{R_C})$, and $(y_{R_C} - z_{R_C})$ planes respectively.

Figure 4 shows the bounds in the radial, along-track motion, and the cross-track motion. The corresponding values (dotted lines) of these bounds are plotted in Fig. 5. The extreme values calculated analytically are able to successfully predict the inner and outer boundaries, with maximum errors in the three directions being less than 0.12%, 0.09% and 0.0002% respectively.

5.2 1:1 commensurable case

In this case, the semimajor axis of the deputy's elliptic displaced orbit is assumed to be $a_D = a_C$, in order to obtain $n_D = n_C$ (1:1 commensurable case). The relevant data are shown in Tab. 3, and the deputy is assumed to track the Mercury's heliocentric orbit with a constant displacement.

Table 4 shows the extreme values of each component of the relative position vector, whereas Fig. 6 shows the relative motion generated by the first-order approximation (dashed lines) and the exact solution (solid lines). The relative motion exhibits periodicity since the mean motions are 1:1 commensurable and, notably, the first-order solution fits well the numerical solution. In particular, the proposed methodology for determining extreme values via first-order approximate solution is accurate in predicting the distance bounds, with maximum errors in

the three directions being less than 0.44%, 0.79% and 0.13% respectively, see also Fig. 7.

Since the approximate extreme values of relative distances are calculated under the "small eccentricity" assumption, it is necessary to check the accuracy of the results as a function of the orbital eccentricity of chief spacecraft. To this end, define the maximum relative distance errors along the three directions, i.e. the maximum differences of the results obtained by using the semi-analytical method and the (exact) numerical method (denoted by subscript "n")

$$\epsilon_i \triangleq \max \left| \frac{\rho_i^\star - \rho_{i_\mathrm{n}}}{\rho_{i_\mathrm{n}}} \right| \qquad \text{with} \qquad i = \{x,\, y,\, z\} \tag{75}$$

Figure 8 illustrates the relative distance errors by varying the chief's eccentricity in a range $e_C \in [0,\, 0.5]$, whereas the deputy's eccentricity is assumed the same as that of Mercury, i.e. $e_D = 0.2056$. Note, however, that even though the approximate solution is able to get the relative distance bounds with a good accuracy, the approximate solution gradually becomes unable to track the relative orbit as e_C approaches 0.1, see Fig. 9. The maximum errors of the estimated bounds, defined in Eq. (75), are essentially different from the maximum errors of the approximate solution, the latter representing the maximum errors along the whole trajectory. As such they do not necessarily obey to a certain monotonously-increasing function of the chief's eccentricity. In other words, the estimated bounds are just some critical points that belong to the approximate solution.

6 Conclusions

The relative motion between elliptic displaced orbits has been parameterized via a set of newly defined orbital elements, and a semi-analytical approach for the evaluation of the relative distance has been discussed. In this context, the relative motion evolves along its invariant manifold and exhibits periodicity (quasi-periodicity) for the commensurable (incommensurable) case.

For the incommensurable case, by conducting the partial derivatives of the directional components with respect to both the chief's true anomaly and deputy's eccentric anomaly, the extreme values of relative distances are found as the real roots of a set of algebraic equations. For the 1:1 commensurable case, a Fourier series expansion is adopted to obtain a first-order time-explicit approximate solution, which is used to seek the bounds by differentiating the directional components of the position vector with respect to time. In this case, the extreme values for the radial and along-track motion are the real roots of a sextic equation, whereas in the cross-track motion, they satisfy a quartic equation. In principle, the discussed methodology is independent of the primary body. In other terms, the semi-analytical relations of the paper can be applied both in a planetocentric and in a heliocentric case.

The illustrative examples have shown that the discussed approach is capable of successfully predicting the inner and outer bounds of relative motion between elliptic displaced orbits. Therefore, the semi-analytical calculation of these bounds is useful for onboard control when the relative motion arrives at the pre-designed boundary. A natural extension of this work is to use the results of the commensurable scenario, in terms of bounds of relative distances, to design periodic motion for formation flying.

7 Acknowledgements

This work was funded by the National Natural Science Foundation of China (No. 11472213) and Open Research Foundation of Science and Technology in Aerospace Flight Dynamics Laboratory of China (No. 2015afdl016). This work was also supported by Chinese Scholarship Council.

Appendix

The entries T_{ij} of matrix $\mathbb{T}_{P_D P_C}$, as a function of the orbital elements of the two displaced orbits, are:

$$T_{11} = (\cos\omega_C \cos\omega_D + \sin\omega_C \sin\omega_D \cos i_C \cos i_D)\cos(\Omega_C - \Omega_D) + (\cos\omega_C \sin\omega_D \cos i_D - \sin\omega_C \cos\omega_D \cos i_C)\sin(\Omega_C - \Omega_D) + \sin\omega_C \sin\omega_D \sin i_C \sin i_D \tag{76}$$

$$T_{12} = (\sin\omega_C \cos\omega_D \cos i_C \cos i_D - \cos\omega_C \sin\omega_D)\cos(\Omega_C - \Omega_D) + (\sin\omega_C \sin\omega_D \cos i_C + \cos\omega_C \cos\omega_D \cos i_D)\sin(\Omega_C - \Omega_D) + \sin\omega_C \cos\omega_D \sin i_C \sin i_D \tag{77}$$

$$T_{13} = \cos\omega_C \sin i_D \sin(\Omega_D - \Omega_C) - \sin\omega_C \cos i_C \sin i_D \cos(\Omega_C - \Omega_D) + \sin\omega_C \sin i_C \cos i_D \tag{78}$$

$$T_{21} = (\sin\omega_C \sin\omega_D \cos i_D + \cos\omega_C \cos\omega_D \cos i_C)\sin(\Omega_D - \Omega_C) + (\cos\omega_C \sin\omega_D \cos i_C \cos i_D - \sin\omega_C \cos\omega_D)\cos(\Omega_C - \Omega_D) + \cos\omega_C \sin\omega_D \sin i_C \sin i_D \tag{79}$$

$$T_{22} = (\sin\omega_C \sin\omega_D + \cos\omega_C \cos\omega_D \cos i_C \cos i_D)\cos(\Omega_C - \Omega_D) + (\sin\omega_C \cos\omega_D \cos i_D - \cos\omega_C \sin\omega_D \cos i_C)\sin(\Omega_D - \Omega_C) + \cos\omega_C \cos\omega_D \sin i_C \sin i_D \tag{80}$$

$$T_{23} = \sin\omega_C \sin i_D \sin(\Omega_C - \Omega_D) - \cos\omega_C \cos i_C \sin i_D \cos(\Omega_C - \Omega_D) + \cos\omega_C \sin i_C \cos i_D \tag{81}$$

$$T_{31} = \cos\omega_D \sin i_C \sin(\Omega_C - \Omega_D) - \sin\omega_D \sin i_C \cos i_D \cos(\Omega_C - \Omega_D) + \sin\omega_D \cos i_C \sin i_D \tag{82}$$

$$T_{32} = \sin\omega_D \sin i_C \sin(\Omega_D - \Omega_C) - \cos\omega_D \sin i_C \cos i_D \cos(\Omega_C - \Omega_D) + \cos\omega_D \cos i_C \sin i_D \tag{83}$$

$$T_{33} = \sin i_C \sin i_D \cos(\Omega_C - \Omega_D) + \cos i_C \cos i_D \tag{84}$$

The coefficients in Eqs. (44)–(46) are:

$$\sigma_0 = -H_D T_{13} e_C - a_C + a_D T_{11}/2 + b_D T_{22}/2 \tag{85}$$

$$\sigma_c = -5a_D T_{11} e_D/4 + H_D T_{13} + a_C e_C - a_D T_{11} e_C/2 + b_D T_{22} e_D/4 + b_D T_{22} e_C/2 \tag{86}$$

$$\sigma_s = -7a_D T_{21} e_D/4 + H_D T_{23} - 3b_D T_{12} e_C/2 + b_D T_{12} e_D/4 + a_D T_{21} e_C/2 \tag{87}$$

$$\sigma_{c2} = H_D T_{13} e_C + a_D T_{11}/2 - b_D T_{22}/2 \tag{88}$$

$$\sigma_{s2} = H_D T_{23} e_C + b_D T_{12}/2 + a_D T_{21}/2 \tag{89}$$

$$\sigma_{c3} = a_D T_{11} e_D/4 + a_D T_{11} e_C/2 - b_D T_{22} e_D/4 - b_D T_{22} e_C/2 \tag{90}$$

$$\sigma_{s3} = b_D T_{12} e_D/4 + a_D T_{21} e_C/2 + a_D T_{21} e_D/4 + b_D T_{12} e_C/2 \tag{91}$$

$$\tau_0 = -H_D T_{23} e_C + a_D T_{21}/2 - b_D T_{12}/2 \tag{92}$$

$$\tau_c = -5a_D T_{21} e_D/4 + H_D T_{23} - a_D T_{21} e_C/2 - b_D T_{12} e_D/4 - b_D T_{12} e_C/2 \tag{93}$$

$$\tau_s = 7a_D T_{11} e_D/4 - H_D T_{13} - 3b_D T_{22} e_C/2 + b_D T_{22} e_D/4 - a_D T_{11} e_C/2 \tag{94}$$

$$\tau_{c2} = H_D T_{23} e_C + a_D T_{21}/2 + b_D T_{12}/2 \tag{95}$$

$$\tau_{s2} = -H_D\, T_{13}\, e_C + b_D\, T_{22}/2 - a_D\, T_{11}/2 \tag{96}$$

$$\tau_{c3} = a_D\, T_{21}\, e_D/4 + a_D\, T_{21}\, e_C/2 + b_D\, T_{12}\, e_D/4 + b_D\, T_{12}\, e_C/2 \tag{97}$$

$$\tau_{s3} = b_D\, T_{22}\, e_D/4 - a_D\, T_{11}\, e_C/2 - a_D\, T_{11}\, e_D/4 + b_D\, T_{22}\, e_C/2 \tag{98}$$

$$\xi_0 = -3\, a_D\, T_{31}\, e_D/2 + H_D\, T_{33} - H_C \tag{99}$$

$$\xi_c = a_D\, T_{31} \tag{100}$$

$$\xi_s = b_D\, T_{32} \tag{101}$$

$$\xi_{c2} = a_D\, T_{31}\, e_D/2 \tag{102}$$

$$\xi_{s2} = b_D\, T_{32}\, e_D/2 \tag{103}$$

References

Aliasi, G., Mengali, G., Quarta, A. A., July 2015. Special orbits for Mercury observation. In: Badescu, V., Zacny, K. (Eds.), Inner Solar System: Prospective Energy and Material Resources. Springer International Publishing, Ch. 5, pp. 101–126, ISBN: 978-3-319-19568-1.

Baoyin, H., McInnes, C. R., Solar sail orbits at artificial sun-earth libration points. J. Guidance Control Dyn. 28 (6), 1328–1331, doi: 10.2514/1.14598, 2005.

Baoyin, H., McInnes, C. R., Solar sail equilibria in the elliptical restricted three-body problem. J. Guidance Control Dyn. 29 (3), 538–543, doi: 10.2514/1.15596, 2006a.

Baoyin, H., McInnes, C. R., Solar sail halo orbits at the sun-earth artificial L_1 point. Celest. Mech. Dyn. Astr. 94 (2), 155–171, doi: 10.1007/s10569-005-4626-3, 2006b.

Battin, R. H., An Introduction to the Mathematics and Methods of Astrodynamics. AIAA, New York, pp. 203–210, 485, ISBN: 1-563-47342-9, 1987.

Ceriotti, M., Heiligers, J., McInnes, C. R., Trajectory and spacecraft design for a pole-sitter mission. J. Spacecraft Rockets 51 (1), 311–326, doi: 10.2514/1.A32477, 2014.

Gong, S., Baoyin, H., Li, J., Solar sail formation flying around displaced solar orbits. J. Guidance Control Dyn. 30 (4), 1148–1152, doi: 10.2514/1.24315, 2007a.

Gong, S., Baoyin, H., Li, J., Relative orbit design and control of formation around displaced solar orbits. Aerosp. Sci. Technol. 12 (2), 195–201, doi: 10.1016/j.ast.2007.05.004, 2008a.

Gong, S., Li, J., Solar sail halo orbit control using reflectivity control devices. Trans. Jpn. Soc. Aeronaut. Space Sci. 57 (5), 279–288, doi: 10.2322/tjsass.57.279, 2014.

Gong, S., Li, J., Baoyin, H., Formation around planetary displaced orbit. Appl. Math. Mech-Engl 28 (6), 759–767, doi: 10.1007/s10483-007-0606-y, 2007b.

Gong, S., Li, J., Baoyin, H., Analysis of displaced solar sail orbits with passive control. J. Guidance Control Dyn. 31 (3), 782–785, doi: 10.2514/1.32360, 2008b.

Gong, S., Yunfeng, G., Li, J., Solar sail formation flying on an inclined earth orbit. Acta Astronaut. 68 (1-2), 226–239, doi: 10.1016/j.actaastro.2010.08.022, 2011.

Gurfil, P., Kholshevnikov, K. V., Manifolds and metrics in the relative spacecraft motion problem. J. Guidance Control Dyn. 29 (4), 1004–1010, doi: 10.2514/1.15531, 2006.

Hu, T., Gong, S., Mu, J. et al., Switch programming of reflectivity control devices for the coupled dynamics of a solar sail. Adv. Space Res. 57 (5), 1147–1158, doi: 10.1016/j.asr.2015.12.029, 2016.

Janhunen, P., Electric sail for spacecraft propulsion. J. Propul. Power 20 (4), 763–764, doi: 10.2514/1.8580, 2004.

Johnson, L., Whorton, M., Heaton, A. et al., NanoSail-D: A solar sail demonstration mission. Acta Astronaut. 68 (5-6), 571–575, doi: 10.1016/j.actaastro.2010.02.008, 2011a.

Johnson, L., Young, R., Barnes, N. et al., Solar sails: Technology and demonstration status. Int. J Aeronaut. Space 13 (4), 421–427, doi: 10.5139/IJASS.2012.13.4.421, 2012.

Johnson, L., Young, R., Montgomery, E. et al., Status of solar sail technology within NASA. Adv. Space Res. 48 (11), 1687–1694, doi: 10.1016/j.asr.2010.12.011, 2011b.

Matloff, G. L., Graphene, the ultimate interstellar solar sail material? JBIS-J. Brit. Interpla. 65, 378–381 , 2012.

McInnes, C. R., The existence and stability of families of displaced two-body orbits. Celest. Mech. Dyn. Astr. 67 (2), 167–180, doi: 10.1023/A:1008280609889, 1997.

McInnes, C. R., Passive control of displaced solar sail orbits. J. Guidance Control Dyn. 21 (6), 975–982, doi: 10.2514/2.4334, 1998.

McInnes, C. R., Solar Sailing: Technology, Dynamics and Mission Applications. Springer-Praxis Series in Space Science and Technology. Springer-Verlag, Berlin, Ch. 5, 1999.

McInnes, C. R., McDonald, A. J. C., Simmons, J. F. L. et al., Solar sail parking in restricted three-body systems. J. Guidance Control Dyn. 17 (2), 399–406, doi: 10.2514/3.21211, 1994.

McInnes, C. R., Simmons, J. F. L., Solar sail halo orbits I: Heliocentric case. J. Spacecraft Rockets 29 (4), 466–471, doi: 10.2514/3.25487, 1992a.

McInnes, C. R., Simmons, J. F. L., Solar sail halo orbits II: Geocentric case. J. Spacecraft Rockets 29 (4), 472–479, doi: 10.2514/3.55639, 1992b.

McKay, R. J., Macdonald, M., Biggs, J. et al., Survey of highly-non-Keplerian orbits with low-thrust propulsion. J. Guidance Control Dyn. 34 (3), 645–666, doi: 10.2514/1.52133, 2011.

Mengali, G., Quarta, A. A., Non-Keplerian orbits for electric sails. Celest. Mech. Dyn. Astr. 105 (1–3), 179–195, doi: 10.1007/s10569-009-9200-y, 2009.

Mingotti, G., Topputo, F., Bernelli-Zazzera, F., Transfers to distant periodic orbits around the moon via their invariant manifolds. Acta Astronaut. 79, 20–32, doi: 10.1016/j.actaastro.2012.04.022, 2012.

Mori, O., Tsuda, Y., Shirasawa, Y. et al., Attitude control of IKAROS solar sail spacecraft and its flight results. In: 61st International Astronautical Congress. Prague, Czech Republic, paper IAC-10.C1.4.3, September 27–October 1 2010.

Mu, J., Gong, S., Li, J., Coupled control of reflectivity modulated solar sail for Geosail formation flying. J. Guidance Control Dyn. 38 (4), 740–751, doi: 10.2514/1.G000117, 2015a.

Mu, J., Gong, S., Ma, P. et al., Dynamics and control of flexible spinning solar sails under reflectivity modulation. Adv. Space Res. 56 (8), 1737–1751, doi: 10.1016/j.asr.2015.07.028, 2015b.

Prado, J.-Y., Perret, A., Pignolet, G., Using a solar sail for a plasma storm early warning system. In: Burke, W., Guyenne, T. D. (Eds.), Environment Modelling for Space-based

Applications. No. ESA SP-392. ESTEC Noordwijk, pp. 213–223, September 18–20 1996.

Topputo, F., Fast numerical approximation of invariant manifolds in the circular restricted three-body problem. Commun. Nonlinear Sci. 32, 89–98, doi: 10.1016/j.cnsns.2015.08.004, 2016.

Tsuda, Y., Mori, O., Funase, R. et al., Achievement of IKAROS - japanese deep space solar sail demonstration mission. In: Genta, G. (Ed.), Missions to the Outer Solar System and Beyond. Seventh IAA Symposium on Realistic Near-Term Advanced Scientific Space Missions, Aosta, Italy, July, 11-13 2011a.

Tsuda, Y., Mori, O., Funase, R. et al., Flight status of IKAROS deep space solar sail demonstrator. Acta Astronaut. 69 (9-10), 833–840, doi: 10.1016/j.actaastro.2011.06.005, 2011b.

Wang, W., Yuan, J. P., Mengali, G. et al., Invariant manifold and bounds of relative motion between heliocentric displaced orbits. J. Guidance Control Dyn., in press, doi:10.2514/1.G001751, 2016.

List of Tables

1 Characteristics of the displaced orbits for the incommensurable case. 31

2 Extreme values of the radial, along-track and cross-track distance for the incommensurable case. 32

3 Characteristics of the displaced orbits for the 1:1 commensurable case. 33

4 Extreme values of the radial, along-track and cross-track bounds for the 1:1 commensurable case. 34

Table 1
Characteristics of the displaced orbits for the incommensurable case.

	a [DU]	H [DU]	e	i [deg]	Ω [deg]	ω [deg]	f [deg]
chief	1	0.1	0.05	0.001	0	0	0
deputy	1.02	0.08	0.2	5	5	0	0

Table 2
Extreme values of the radial, along-track and cross-track distance for the incommensurable case.

component	$\iota^\star$	$\upsilon^\star$	$f_C^\star \mod \pi$ [rad]	$E_D^\star \mod \pi$ [rad]	extreme values [DU]	
ρ_x	0.0971	0.0519	0.1935	0.1037	0.1743	−2.1742
ρ_y	−1.4379	0.0445	1.7028	0.0437	1.2241	−1.2241
ρ_z	-	-	-	1.5708	0.0668	−0.1074

Table 3
Characteristics of the displaced orbits for the 1:1 commensurable case.

	a [DU]	H [DU]	e	i [deg]	Ω [deg]	ω [deg]	f [deg]
chief	1	0.1	0.05	0.001	50	80	0
deputy	1	0.08	0.2056	7	48.33	77.45	0

Table 4
Extreme values of the radial, along-track and cross-track bounds for the 1:1 commensurable case.

component	$s^\star$		$t^\star \bmod 2\,\pi$ [TU]		extreme values [DU]	
ρ_x	21.7824	−0.0968	3.0498	6.0902	0.1549	−0.1740
ρ_y	−1.0057	0.9192	1.4866	4.7067	0.2480	−0.3896
ρ_z	−6.9272	0.0919	0.1833	3.4283	0.0768	−0.1671

List of Figures

1 Reference frames. 36

2 Displaced orbits of chief and deputy spacecraft. 37

3 Three-dimensional incommensurable relative motion with its invariant manifold $\mathfrak{R}$. 38

4 Projections of incommensurable relative trajectory on $(x_{R_C} - y_{R_C})$, $(x_{R_C} - z_{R_C})$, and $(y_{R_C} - z_{R_C})$ planes. 39

5 Analytic bounds (dotted lines) and numerical simulation (solid line) of relative motion for the incommensurable case. 40

6 Relative motion: comparison of the first-order approximation and the exact solution. 41

7 Approximate semi-analytic bounds and simulated directional relative motion for the 1:1 commensurable case. 42

8 Maximum relative distance errors ϵ_i along the three directions, see Eq. (75). 43

9 Three dimensional relative motion as a function of chief's orbital eccentricity e_C. 44

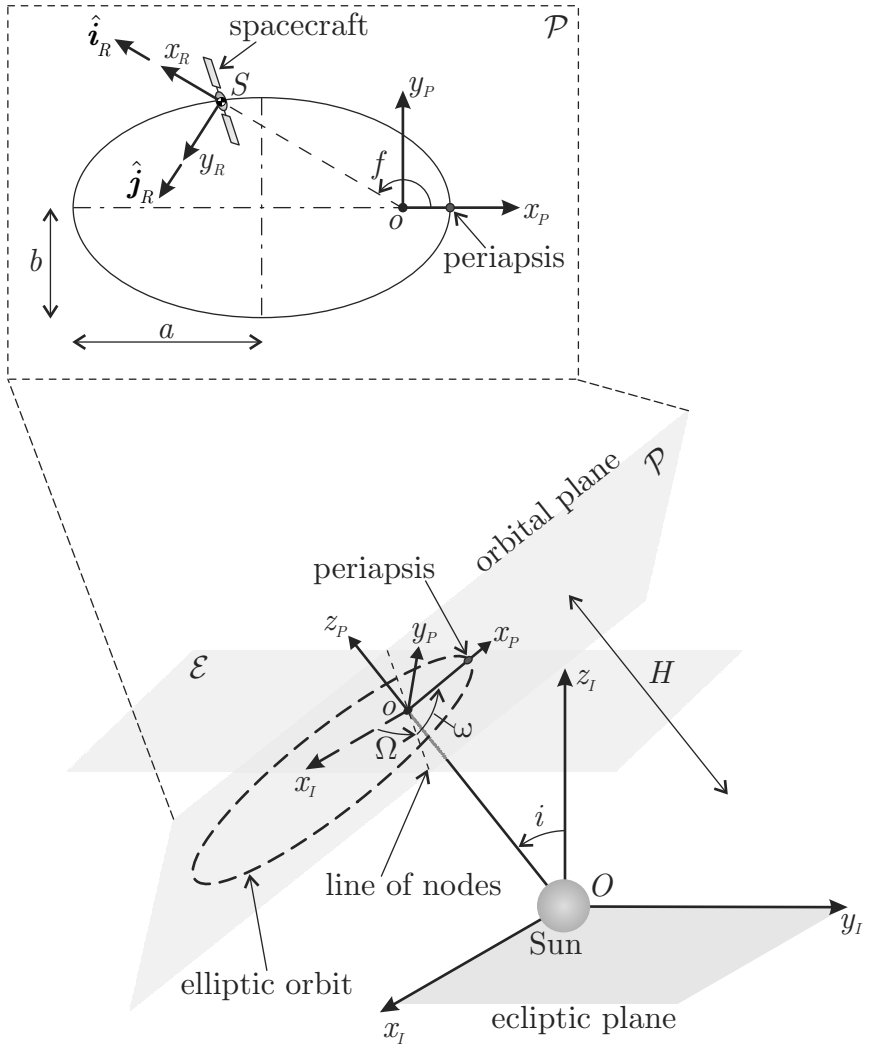

Fig. 1. Reference frames.

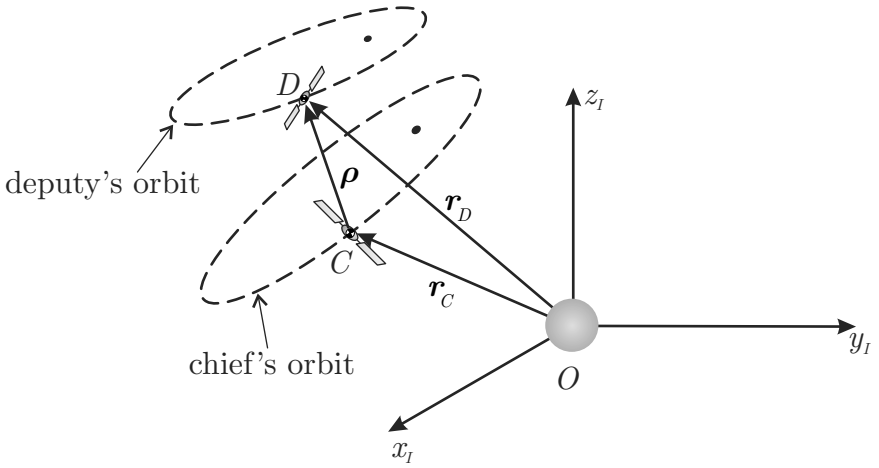

Fig. 2. Displaced orbits of chief and deputy spacecraft.

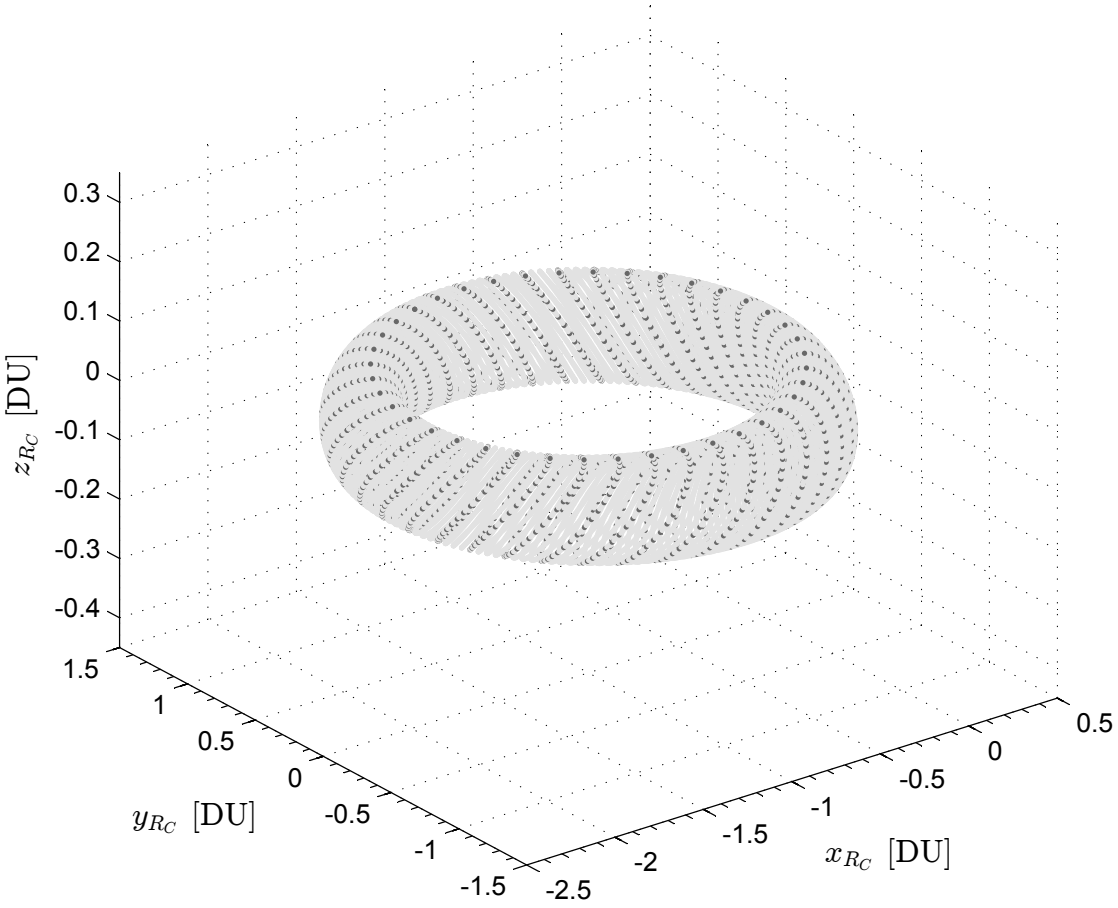

Fig. 3. Three-dimensional incommensurable relative motion with its invariant manifold $\mathfrak{R}$.

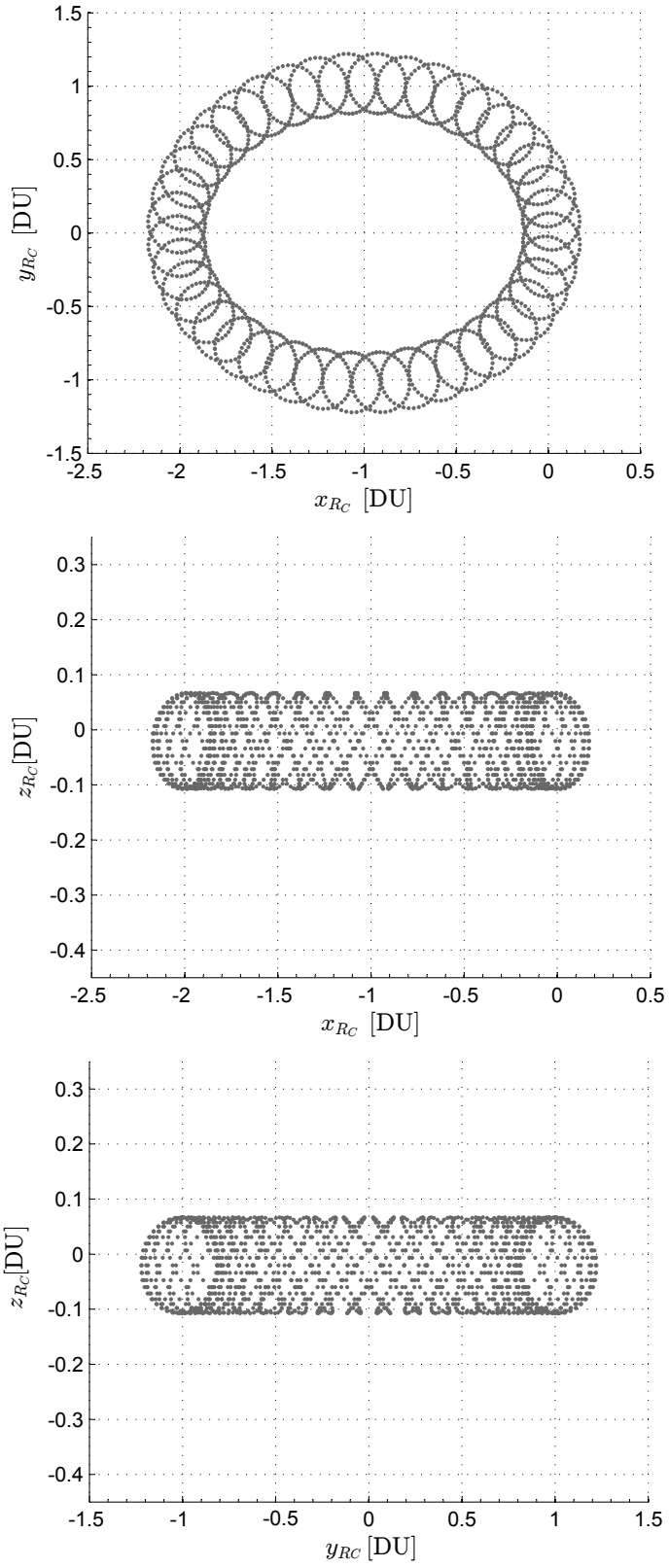

Fig. 4. Projections of incommensurable relative trajectory on $(x_{R_C} - y_{R_C})$, $(x_{R_C} - z_{R_C})$, and $(y_{R_C} - z_{R_C})$ planes.

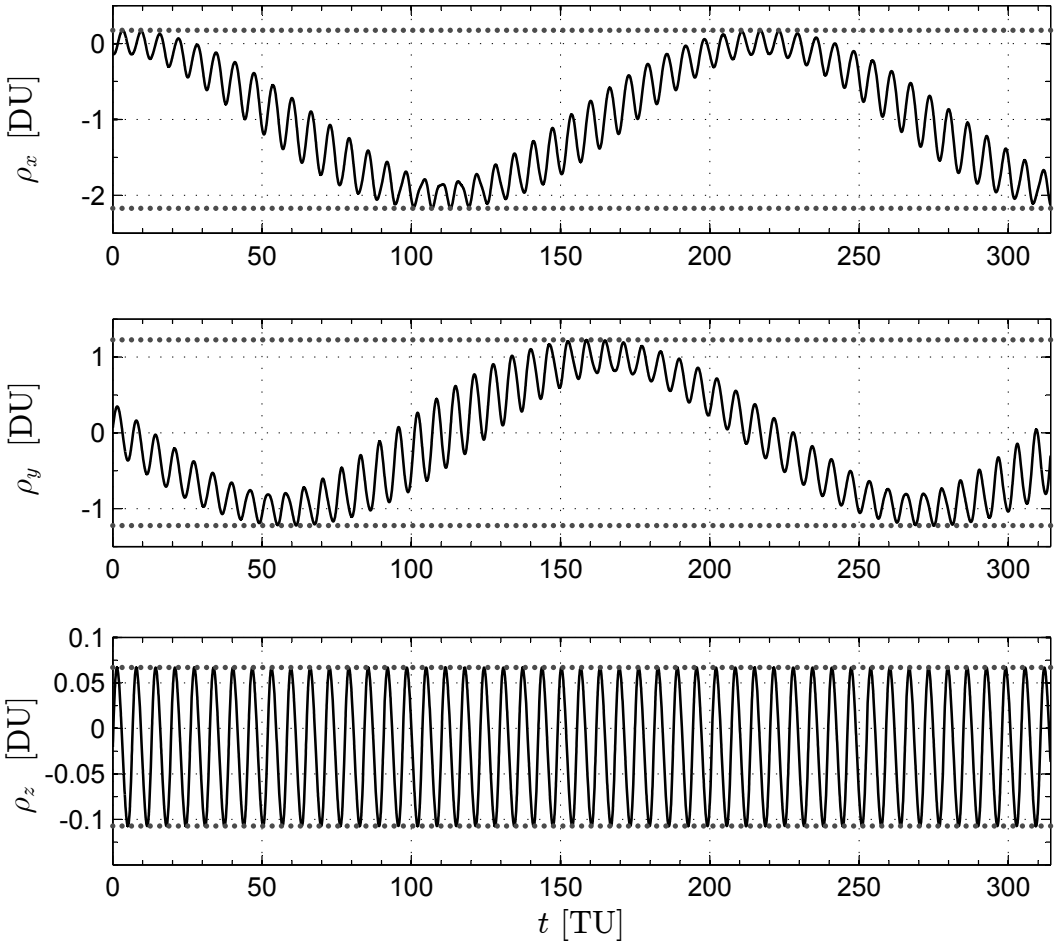

Fig. 5. Analytic bounds (dotted lines) and numerical simulation (solid line) of relative motion for the incommensurable case.

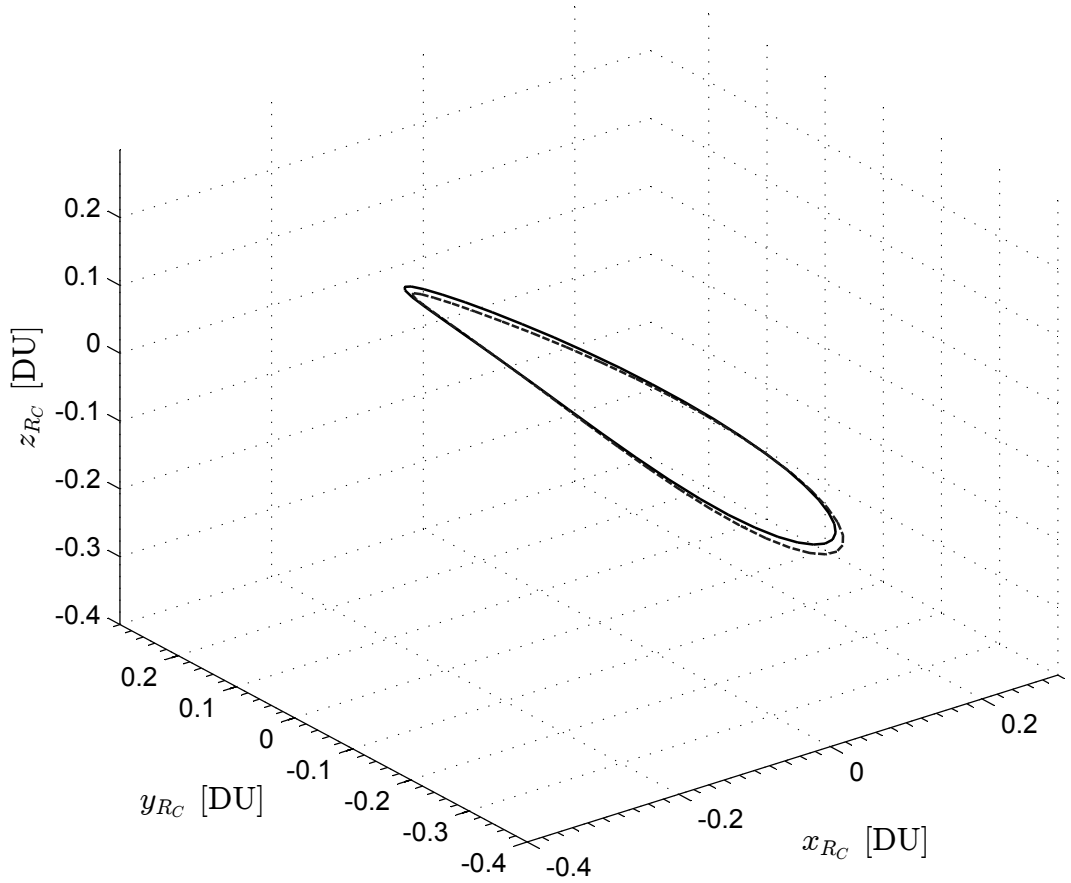

Fig. 6. Relative motion: comparison of the first-order approximation and the exact solution.

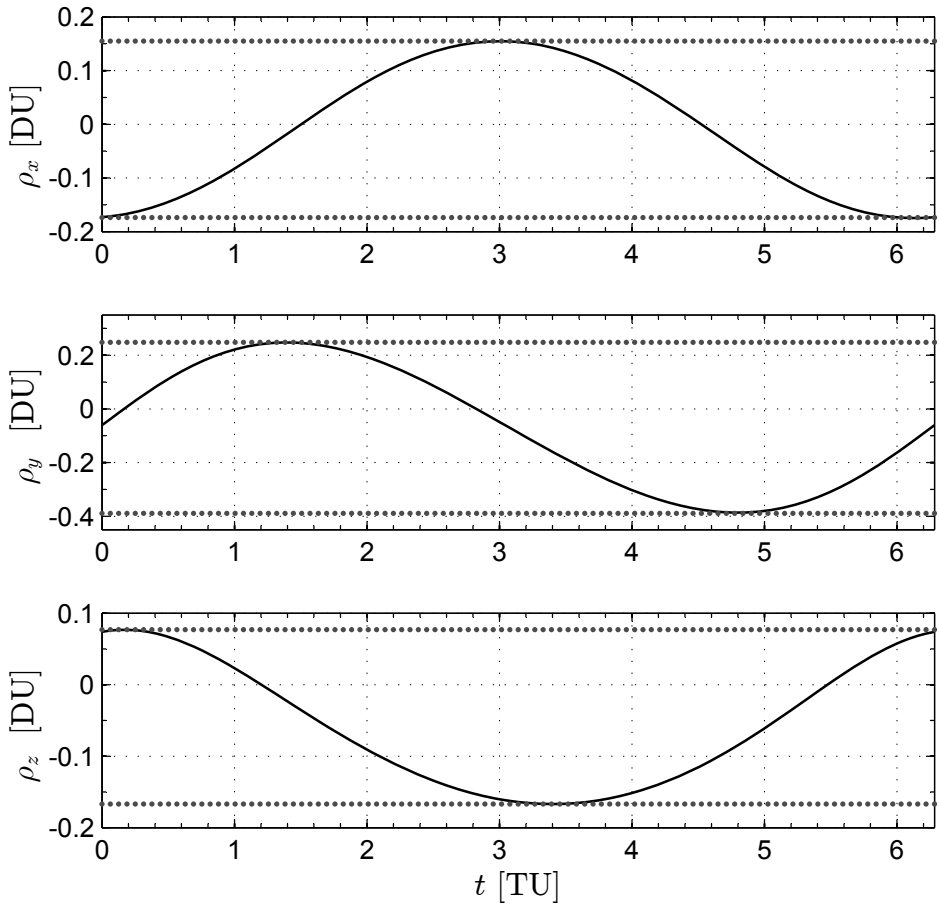

Fig. 7. Approximate semi-analytic bounds and simulated directional relative motion for the 1:1 commensurable case.

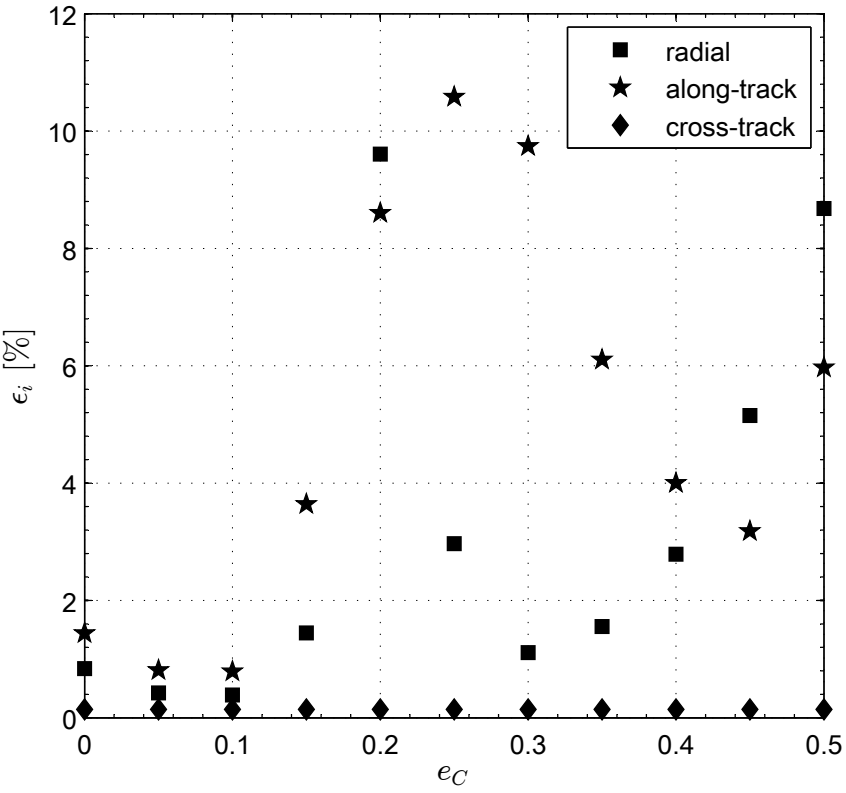

Fig. 8. Maximum relative distance errors ϵ_i along the three directions, see Eq. (75).

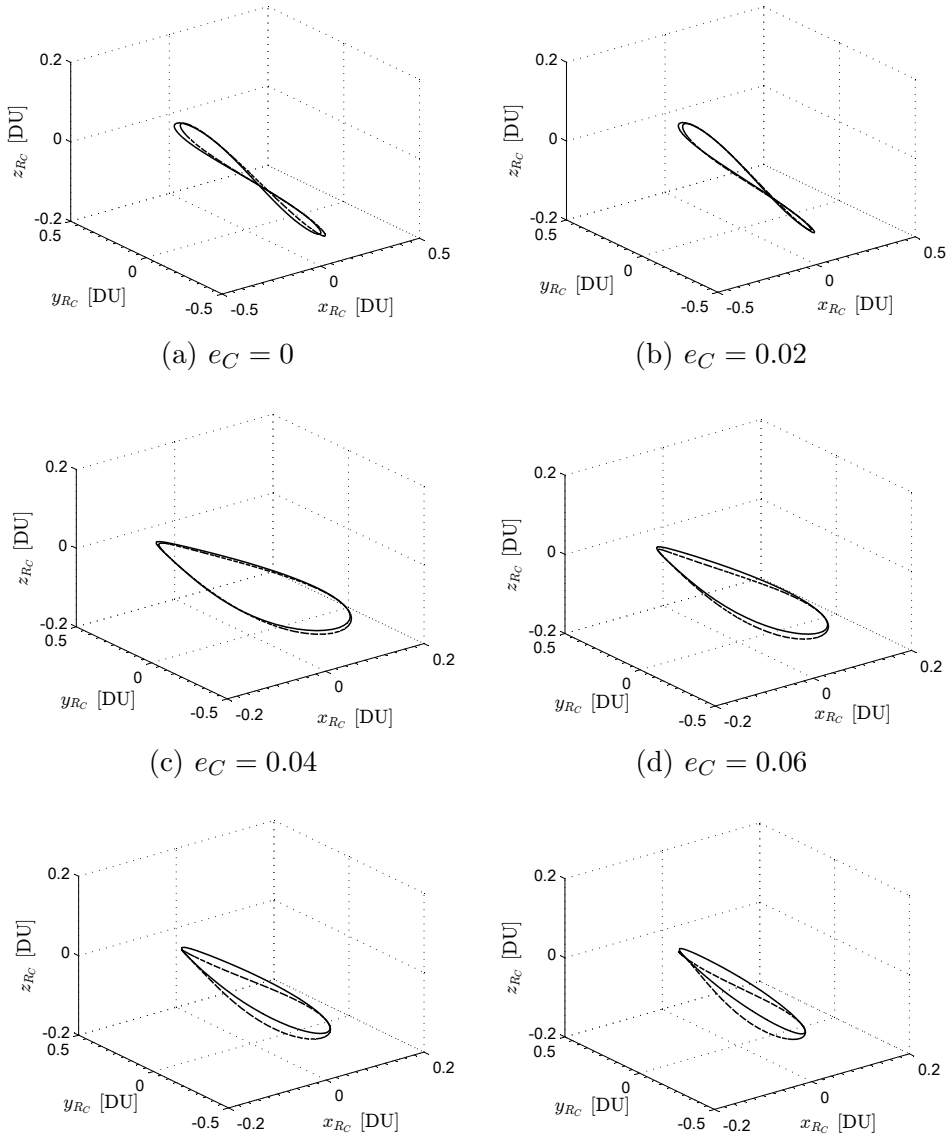

(a) $e_C = 0$ (b) $e_C = 0.02$

(c) $e_C = 0.04$ (d) $e_C = 0.06$

(e) $e_C = 0.08$ (f) $e_C = 0.1$

Fig. 9. Three dimensional relative motion as a function of chief's orbital eccentricity e_C.